In-situ synchrotron X-ray imaging of curved columnar growth and ripple formation in Fe-Mn-Cr-Ni-Si alloy during GTA welding

Tomoya Nagira [a,*], Houichi Kitano [a] Takashi Kimura [a], Fumiyoshi Yoshinaka [a], Susumu Takamori [a], Takahiro Sawaguchi [a], Takayuki Yamashita [b], Yasuhiro Aoki [b], Hidetoshi Fujii [b]

[a] National Institute for Materials Science, 1–2–1, Sengen, Tsukuba, Ibaraki, 305–0047, Japan
[b] Joining and Welding Research Institute, Osaka University, 11–1 Mihogaoka, Ibaraki, Osaka, 567–0047, Japan

*Corresponding author: Tel. &FAX: +81-29-859-2408
E-mail: NAGIRA.Tomoya@nims.go.jp (T. Nagira)

Abstract

The dynamics of curved columnar growth and ripple formation in Fe-Mn-Cr-Ni-Si alloys were studied in situ during GTA melt-run welding using synchrotron radiation X-ray imaging with high spatial resolution. In situ observations demonstrated that primary dendrite arm growth ceased when the angle between the growth direction of the primary dendrite arms and the direction of the maximum temperature gradient exceeded 44–49 º at welding speeds of 1–7 mm/s. Consequently, curved columnar grains were formed by changing the growth direction via the development of secondary dendrite arms into primary dendrite arms. Image analysis revealed that a weld ripple, where solutes were highly segregated in the dendrite trunk, was formed by a rapid increase in the interface velocity.

Keywords: In situ observation; X-ray imaging; curved columnar growth; ripple formation; GTA welding

1. Introduction

During the welding process, the microstructure of the weld metal is affected by welding parameters such as welding speed and heat input and is formed through initial epitaxial growth at the fusion line, subsequent dendrite growth, and dendrite competition in the weld pool [1,2]. In melt-run welding, where the heat source moves, various solidification microstructures can form as the weld pool shape varies with the welding speed. At a low welding speed, the weld pool became elliptical, and the columnar dendrites grew continuously with a change in the growth direction as the direction of the maximum thermal gradient changed from perpendicular to the fusion line to parallel to the welding direction during the movement of the heat source. Consequently, the inherent microstructure with curved columnar grains is formed [1,2]. At a high welding speed, columnar grains grew linearly from both sides of the fusion boundary and collided at the center of the weld bead as the weld pool became a teardrop. However, previous studies were based on the observation of fully solidified specimens. To the best of our knowledge, it is not clear how the columnar grains curve at the dendrite scale during arc melt-run welding at a low welding speed, owing to the difficulty of observation under the influence of arc light.

Another inherent solidification phenomenon in the melt-run welding is a formation of ripple, which contains solute segregation and porosity [3–5]. Attorre et al. [4] demonstrated that ripple is influenced by the welding current, welding speed, and sample thickness. Hall et al. [5] conducted an in situ observation of ripple formation using a high-speed camera and showed that the weld ripple was associated with a remarkable change in the solidification velocity. However, the relationship between ripple formation and solidification velocity is lacking despite in situ observations owing to the low spatial resolution. In addition, ripple formation is involved in solute distribution at the solid-liquid interface [3–5]. Dendrite-scale microstructural analysis is also important for elucidating the ripple formation mechanisms.

In situ observation techniques have been widely adopted to examine welding phenomena such as the dynamics of weld pools [6], porosity [7], solidification cracking [8,9], and solidification microstructure, including grain growth and phase transformation [10,11], using synchrotron radiation X-ray diffraction and imaging. In particular, X-ray imaging, which can be used to visualize dynamic phenomena, is a powerful tool for elucidating the formation mechanisms of solidification microstructures, although the observation subject is limited to the dynamics of high-contrast images. In our recent studies, a technique for observing solidification behaviors at the dendrite scale during gas

tungsten arc (GTA) melt-run welding was developed using synchrotron radiation X-ray imaging with a high spatial resolution [12]. This technique enabled us to directly observe the microstructural evolution, such as columnar and equiaxed dendrite growth during welding. Previous studies [12] visualized the initiation and propagation of solidification cracking in Fe-Mn-Cr-Ni-Si alloys, which have recently drawn considerable interest for their potential application in seismic steel dampers owing to their remarkable plastic fatigue life [13]. The cracking behavior is closely related to the impingement of columnar dendrites and dendrite morphology. Therefore, dendrite-scale in situ observations using the developed technique are expected to provide new insights into curved columnar grain growth and ripple formation. These findings are useful for developing reliable models [14] and simulations [15] of microstructural evolution in weld metals.

This study focuses on directly observing the columnar dendrite growth of Fe-Mn-Cr-Ni-Si alloys during GTA melt-run welding using high-spatial-resolution synchrotron radiation X-ray imaging. The formation mechanism of the curved columnar grains was examined from the perspective of the angle between the growth direction and the direction of the maximum temperature gradient, and the growth velocity at various welding speeds. The relationship between the solid-liquid interface velocity and weld ripple was examined using detailed image analysis to clarify the mechanism of ripple formation.

2. Experimental Procedures

An alloy with a nominal composition of Fe-15Mn-10Cr-8Ni-4Si, which solidifies in the austenite mode [12], was used to observe the dendrite growth of austenite. The alloy was fabricated in an induction furnace under an Ar atmosphere, hot-forged at 1100 °C, and rolled into plates. Heat treatment was then conducted at 1000 °C for 1 h, followed by quenching in water. The dimensions of the sample were 50 mm length, 50 mm width, and 0.2 mm thickness.

In situ experiments were performed at the imaging beamline 20XU of SPring-8, Japan. A schematic illustration of the experimental setup for the in situ observations during GTA melt-run welding is shown in Figure 1. An X-ray imaging detector, GTA welding apparatus, a specimen cell, and a high-speed camera were placed along the X-ray path. Transmitted X-ray images were obtained at an X-ray energy of 28 keV. The narrow visual field lens where the observation area was 1.0 mm × 1.0 mm with a pixel size of 0.49 μm was used for the in-situ observation of dendrite growth. The wide visual field lens where the observation area was 2.2 mm × 2.2 mm with a pixel size of 1.1 μm was used for the in-situ observation of ripple formation. The frame rate and exposure time for each image were 50 fps and 20 ms, respectively.

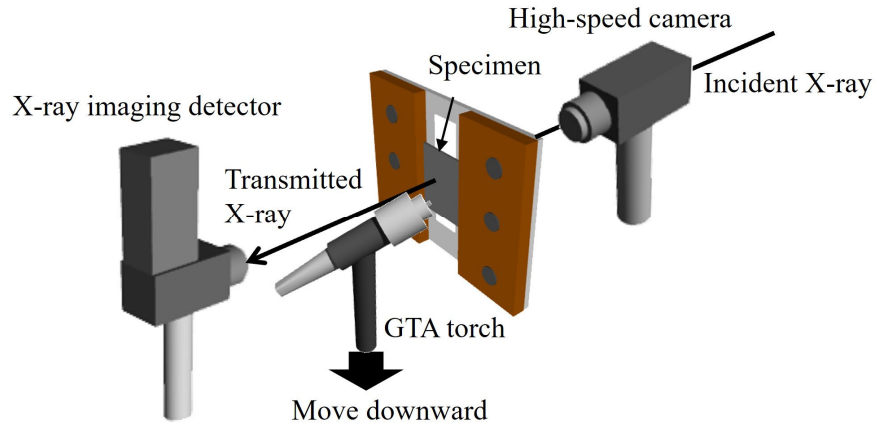

Figure 1. Schematic of the experimental setup for in-situ observation during GTA melt-run welding.

The temperature distribution was measured using a high-speed camera simultaneously with in situ X-ray imaging during GTA melt-run welding. High-speed camera images acquired at 250 fps were converted to temperature images using two-color method software (NAC Image Technology Inc., Thermias).

The specimens were fixed using a Cu plate and an Al backing plate with a hole for the X-rays to pass through. The GTA torch was placed on the z-axis stage. GTA melt-run welding was performed by moving the z-axis stage downward. Argon was used as a shielding gas at a flow rate of 20 L/min. In situ experiments were conducted at five different welding speeds of 1, 3, 5, 7, and 10 mm/s to examine the effect of welding speed on the solidification phenomena. The weld pool fully penetrated under all welding conditions.

The microstructure of the solidified specimen after the in-situ observation was characterized using electron backscattering diffraction (EBSD). An electron probe microanalyzer (EPMA) was used to determine the solute distribution of the weld bead for the specimen quenched with Ar gas after the in situ experiment.

X-ray images were processed to measure solid-liquid interface velocity. Denoising and contrast enhancement employed a self-supervised machine-learning model [16]. Local entropy [17] was calculated from brightness variation within a 32-pixel-radius circular around each pixel. In solids, brightness fluctuated significantly because of solute segregation; hence pixels whose entropy exceeded a threshold were labeled solid and those below, liquid, delineating the interface. The threshold, chosen after careful inspection of entropy distributions, was set to the 42th percentile across all frames. Each interface was fitted with a quadratic curve at every time step. Interface velocity was then

obtained by averaging positions within ±60 pixels of the image center along the weld width; per-pixel velocities over the same ±60 pixel range were likewise computed for quantifying their uncertainties.

3. Results and discussion

3.1 Dendrite growth and competition during GTA melt run welding

Figure 2(a–c) shows X-ray radiographs of dendritic growth at a welding speed of 1 mm/s. A magnified image of the white dotted square in Figure 2(c) is shown in Figure 2(d). The complete time sequence of the dendrite growth is provided in Supplementary Video 1. A nearly circular weld pool was formed immediately after arc ignition. The weld pool shape remained unchanged during GTA melt-run welding because of the low

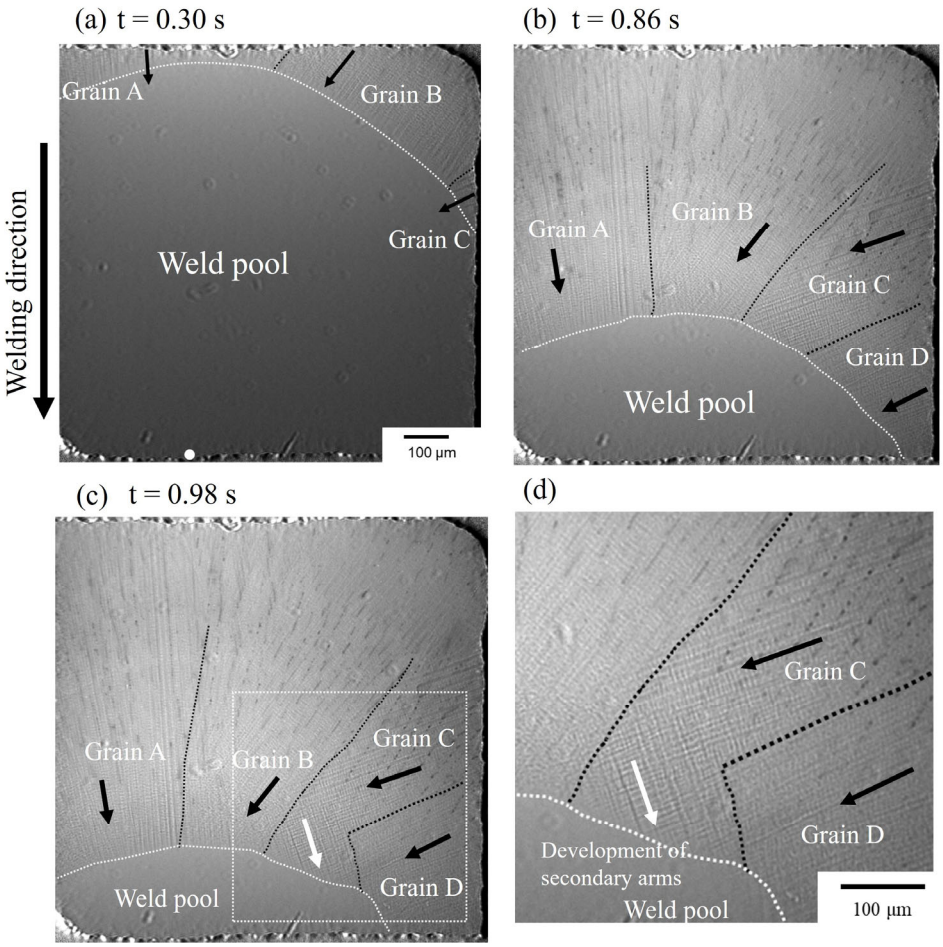

Figure 2. (a–c) X-ray radiographs of the dendritic growth. (d) Magnified image of the white dotted square in (c). The black and white arrows denote the growth directions of primary and secondary dendrite arms, respectively. The white and black dotted lines denote the solid-liquid interface and grain boundary, respectively.

welding speed. Four columnar grains, labeled A–D, were chosen to explain the competitive dendritic growth. At time t = 0.30 s, columnar grains A, B, and C grew toward the center of the circular weld pool. The growth direction of grain C was nearly perpendicular to the welding direction. At t = 0.86 s, the growth of some primary dendrite arms of grain C was blocked by columnar grain B. When the primary dendrite arms for the grain C could no longer grow owing to the blocking of columnar grain B at t = 0.98 s, the secondary dendrite arms were found to develop into new primary dendrite arms (Figure 2(d)). The growth of grain D was blocked by the extension of the secondary dendrite arms for grain C. Consequently, columnar grain C continued to grow while changing its growth direction via the development of secondary dendrites arms.

Figure 3(a–d) shows the X-ray radiographs of the dendritic growth at welding speeds of 3, 5, 7, and 10 mm/s, respectively. The observations focused on the primary dendrite arms, which initially grew in a direction nearly perpendicular to the welding direction under all welding conditions. As in the case of a welding speed of 1 mm/s, the development of secondary dendrite arms into new primary dendrite arms occurred when

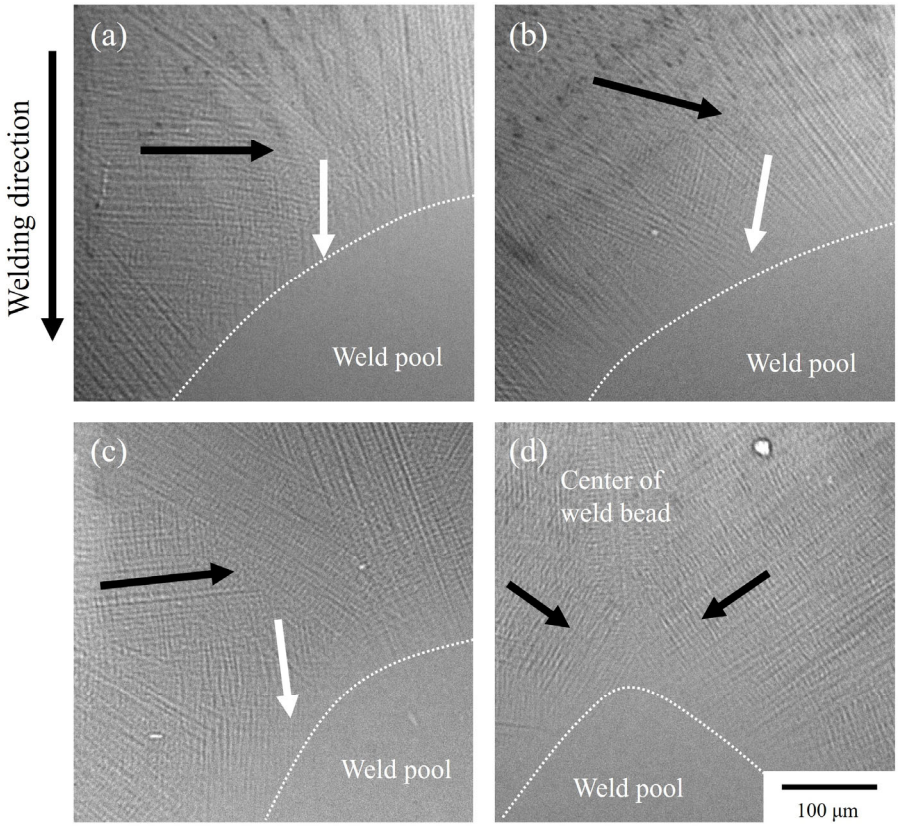

Figure 3. X-ray radiographs of dendritic growth at welding speeds of (a) 3 mm/s, (b) 5 mm/s, (c) 7 mm/s, and (d) 10 mm/s.

the primary dendrite arm growth could no longer occur by blocking other columnar grains at welding speeds of 3–7 mm/s. As the welding speed increased, the weld pool changed from a nearly circular (1 mm/s) shape to an elliptical (3–7 mm/s) shape and further changed to a teardrop (10 mm/s) shape. The primary dendrite arms grew linearly toward the center of the weld bead at a welding speed of 10 mm/s. Columnar dendrites from both sides of the fusion boundary impinged at the center of the weld bead.

3.2 Formation mechanism of curved columnar grains

To clarify the mechanism for the development of secondary dendrite arms at welding speeds of 1–7 mm/s, the angle θ between the growth direction of primary dendrite arms and the direction of maximum temperature gradient was examined during the columnar dendrite growth. The example of X-ray radiograph showing θ for the grain C is shown in Figure 4(a). The direction of the maximum temperature gradient is generally defined as the direction perpendicular to the tangent of the solid-liquid interface [18]. Figure 4(c,d) shows examples of the camera image and temperature distribution,

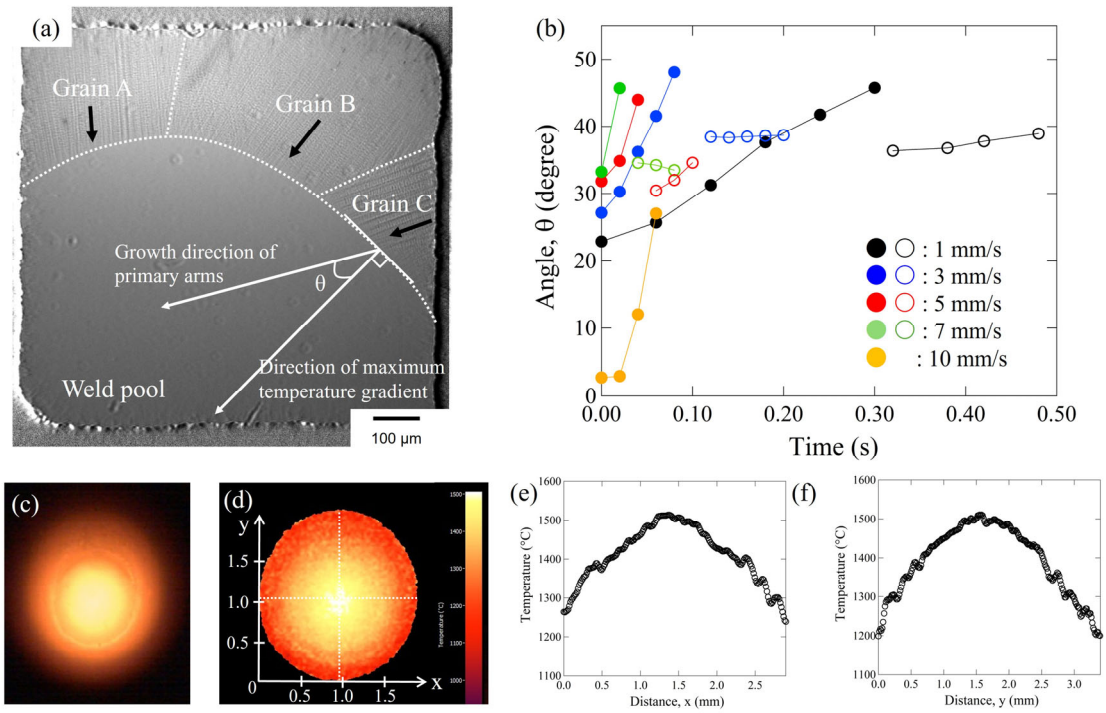

Figure 4. (a) X-ray radiograph showing θ for the grain C. (b) Time dependencies of the angle during primary dendrite arm growth at welding speeds of 1–10 mm/s. The closed and open circles denote the primary and secondary dendrite arms, respectively. An example of (c) camera image, (d) temperature distribution, and temperature profiles at (e) x axis and (f) y axis.

respectively. Temperature measurements indicated that the direction of the maximum temperature gradient was nearly equivalent to the direction perpendicular to the tangent of the solid-liquid interface. The time dependencies of θ during primary dendrite arm growth at welding speeds of 1–10 mm/s are shown in Figure 4(b). For comparison, θ during the growth of secondary dendrite arms after the primary dendrite arms growth no longer occurred is shown. At welding speeds of 1–7 mm/s, the primary dendrite arms continued to grow until θ increased up to the critical value ranging from 44º to 49º. When θ exceeded the critical value, the secondary dendrite arms developed into new primary dendrite arms (Figure 3(a–c)). Previous studies [18,19] have shown that new columnar/equiaxed grains, called stray crystals, are formed ahead of the growing columnar grains at a low welding speed (2 mm/s). Frequent nucleation of stray crystals occurred inside the weld metal when the growth direction of the columnar grains deviated by 35°–45° from the direction of the maximum temperature gradient. In this study, no stray crystal was nucleated inside the weld metal, although the formation condition of stray crystal was satisfied at a similar welding speed.

Columnar dendrites generally tend to grow in the easy-growth direction (<100>) for face-centered cubic (FCC) and body-centered cubic (BCC) metals, and the direction of the dendrites aligns closely with the direction of maximum heat flow [20]. Therefore, the growth of primary dendrite arms with higher θ than 44°–49° was entirely blocked via the dendrite competition (Figure 2). When the secondary dendrite arms began to develop, θ of secondary dendrite arms were 36.4º, 38.5º, 30.5º, and 34.6º at welding speeds of 1, 3, 5, and 7 mm/s, respectively, which was remarkably smaller than those of the primary dendrite arms. The smaller θ facilitated the growth of dendrite without being blocked by other dendrites.

Meanwhile, a change in the growth direction via the development of secondary dendrite arms did not occur at a welding speed of 10 mm/s. Although θ increased during the growth of primary dendrite arms, the primary dendrite arm tip impinged at the center of the weld bead before θ reached the critical value.

Figure 5 shows the time dependence of the growth velocity at welding speeds of 1–10 mm/s. The temperature gradient at a welding speed of 1 mm/s is shown according to the temperature distributions in Figure 4(e,f). The growth velocities of the primary dendrite arms increased as the interface progressed toward the weld centerline. In general, the growth velocity R is expressed by the following equation [20,21]:

$$R = \frac{V \cos \alpha}{\cos(\alpha - \beta)} \quad (1)$$

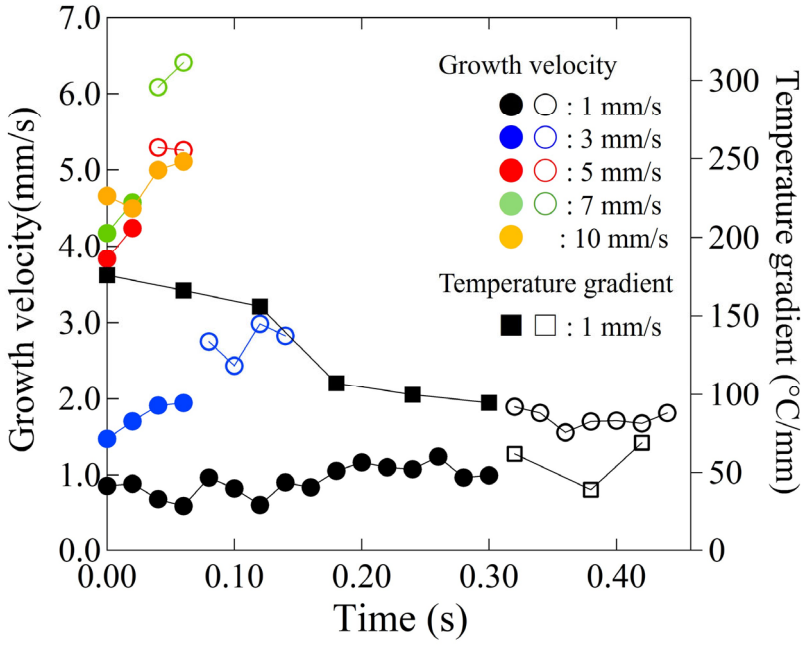

Figure 5. Time dependencies of growth velocity for the primary and secondary dendrite arms at welding speeds of 1–10 mm/s and the temperature gradient at the welding speed of 1 mm/s. The closed and open circles and square denote the primary and secondary dendrite arms, respectively.

Here, V is the welding speed, α is the angle between the welding direction and normal to the weld pool boundary, and β is the angle between the welding direction and the growth direction of the dendrite. If the growth direction equals the normal direction at the weld pool boundary, the difference between α and β is negligible. Equation 1 approximates the following equation.

$$R = V\cos\alpha \qquad (2)$$

Equation 2 indicates that growth velocity reaches the maximum at the weld centerline (α = 0°) and the minimum at the fusion line (α = 90°). Therefore, the growth velocity generally increases as the interface progressed toward the weld centerline owing to the decrease in α. In this study, the difference between α and β corresponds to θ because the normal direction at the weld pool boundary equals the maximum temperature gradient. θ increased from approximately 20° to 50° (Figure 4(a)) as the interface progressed to the weld centerline at welding speeds of 1–7 mm/s. According to Equation 1, a high deviation angle ($\theta = \alpha - \beta$) causes the dendrite to grow faster than the $V\cos\alpha$ [21]. The growth velocity increased with increasing θ (Figure 5).

Meanwhile, the growth velocities of the secondary dendrite arms increased by 1.8,

1.6, 1.4, and 1.4 times compared with those of the primary dendrite arms at welding speeds of 1, 3, 5, and 7 mm/s, respectively. The remarkable increase in the growth velocity of the secondary dendrite arms occurred despite the decrease in θ (Figure 4(b)). The development of secondary dendrite arms was similar to the branching of dendrites during the casting process [20]. The dendrite branching generally occurs in the open region of liquid formed by the growth divergence between the two neighboring grains. Secondary and tertiary dendrite arms extended into the open region of liquid at a higher growth velocity than primary dendrite arms because of high undercooling condition. The development of secondary or tertiary dendrite arms into new primary dendrite trunks occurred [20]. In this study, the primary dendrites arms grew at higher growth velocity than $V\cos\alpha$ because of the high deviation (θ) according to Equation 1. The driving force for primary dendrite arm growth at high growth velocities is high undercooling [20]. Therefore, the secondary dendrite arms extended toward the open region of liquid under high undercooling conditions when the growth of the primary dendrite arms was blocked by other dendrite arms. Subsequently, the secondary dendrite arms with smaller θ became new primary dendrite arms.

At the welding speed of 1 mm/s, the temperature gradient G of the primary dendrite arms gradually decreased from 175 to 95 °C/mm during the growth of primary dendrite arms. The average temperature gradient of the secondary dendrite arms was 56 °C/mm, which was significantly smaller than that of the primary dendrite arms. As the G/R ratio decreases from the fusion boundary toward the weld centerline, a columnar-to-equiaxed transition can occur near the weld centerline owing to an increase in constitutional undercooling [1,22]. In this experiment, G/R decreased remarkably from 205 to 96 °C·s/mm^2 for the primary dendrite arm growth at the welding speed of 1 mm/s. The average G/R of the secondary dendrite arms was 32 °C·s/mm^2. However, no equiaxed dendrites nucleated ahead of the primary and secondary dendrite arms.

Figure 6(a) shows an inverse pole figure (IPF) map of the solidified specimen after the in situ experiment at a welding speed of 1 mm/s. The magnified IPF map of the black dotted square in Figure 6(a) and an optical micrograph are shown in Figure 6(b,c), respectively, where grains A, B, C, and D correspond to those shown in Figure 2. Notably, some grains that were not observed in the X-ray radiograph were observed because some dendrites partially overlapped. The specimen exhibits a conventional microstructure consisting of curved columnar grains (Figure 6(a)). Grain C with a curved morphology was formed by a change in the growth direction from nearly perpendicular to nearly parallel to the welding direction. This resulted from the development of secondary

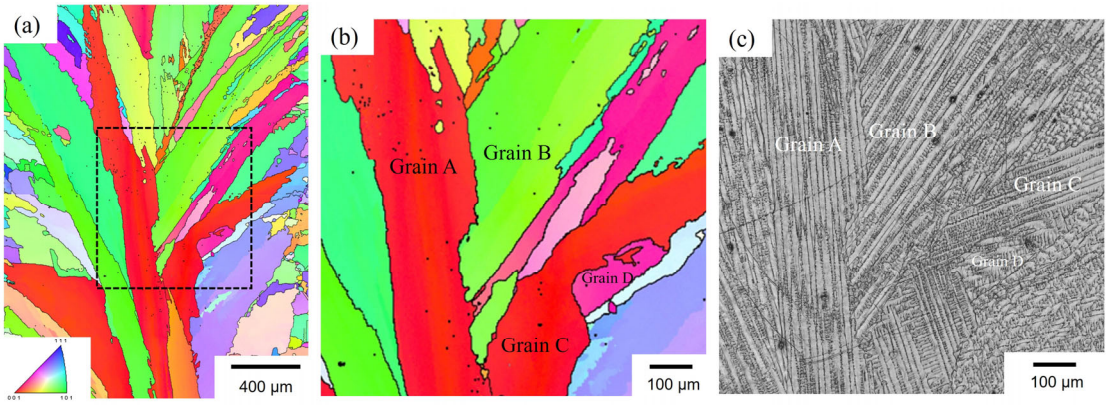

Figure 6. (a) IPF map, (b) magnified image of the black dotted square in (a), and (c) optical micrograph for the solidified specimen.

dendrite arms into new primary dendrite arms. In Figure 6(c), the development of secondary dendrite arms was observed clearly for grain C at the point where the growth direction changed.

When the sample thickness becomes higher than 0.2 mm, it is expected that columnar dendrites tend to grow three-dimensionally. Consequently, the development of higher order dendrite arms likely occurs. It is interesting to examine the effect of the sample thickness on the solidification behavior. This will be the subject of future research.

3.3 Ripple formation during GTA melt-run welding

The transmitted X-ray intensity I is generally expressed by the following equation:

$$I = I_0 \exp\left[-\mu_{specimen} t\right] \qquad (3)$$

where I_0 and t are the incident X-ray intensity and sample thickness, respectively. The linear X-ray absorption coefficient of the specimen for compounds, $\mu_{specimen}$, is given by the following equation:

$$\mu_{specimen} = \rho \sum_i \left(\frac{\mu}{\rho}\right)_i w_i \qquad (4)$$

ρ, (μ/ρ), and w_i are the density, the mass absorption coefficient, and the mass fraction of the constituent element i respectively. Assuming that the sample thickness is constant, the transmitted X-ray intensity depends on the linear X-ray absorption coefficient, which consists of the mass X-ray absorption coefficient and mass density. In Fe-Mn-Cr-Ni-Si alloys, solutes such as Mn, Ni, and Cr have high density and mass-absorption coefficients. The X-ray radiographic images darkened as the solute concentration increased. Therefore, X-ray radiography enabled the recognition of the weld ripple, which corresponded to the solute-enriched band, during solidification.

Figure 7(a–e) shows the sequence of ripple formation at a welding speed of 1 mm/s. The complete time sequence of the ripple formation is provided in Supplementary Video 2. Four weld ripples with darker contrast and semicircular shapes were formed (Nos.1–4). Figure 7(f) shows interface velocity versus time, averaged over ±60 pixels about the center; error bars span maximum–minimum per-pixel velocities within that band. Although the growth of the solid-liquid interface occurred at an average velocity of 1.1 mm/s, the velocity was found to change periodically according to detailed image analysis. In this experiment, GTA welding was conducted without a pulsed current. Therefore, the periodic change in velocity is likely attributable to the oscillation of the weld pool, which is caused by the effects of the arc pressure and electromagnetic force [23]. The formation of the solute-enriched band (No. 3) can be explained as follows: In Figure 7(f), the solid-liquid interface advanced with a nearly constant velocity of 0.88 mm/s between 0.92 and 1.14 s. During this time, no solute-enriched bands were formed (Figure 7(b,c)). After t = 1.14 s, the solid-liquid interface velocity remarkably increased and reached a maximum value of 1.71 mm/s at 1.24 s. During the remarkable increase in the solid-liquid interface velocity, a solute-enriched semicircular band (No. 3) with a darker contrast emerged (Figure 7(d)). Other solute-enriched bands (Nos.1, 2, and 4) also formed during the remarkable increase in the solid-liquid interface velocity. When the

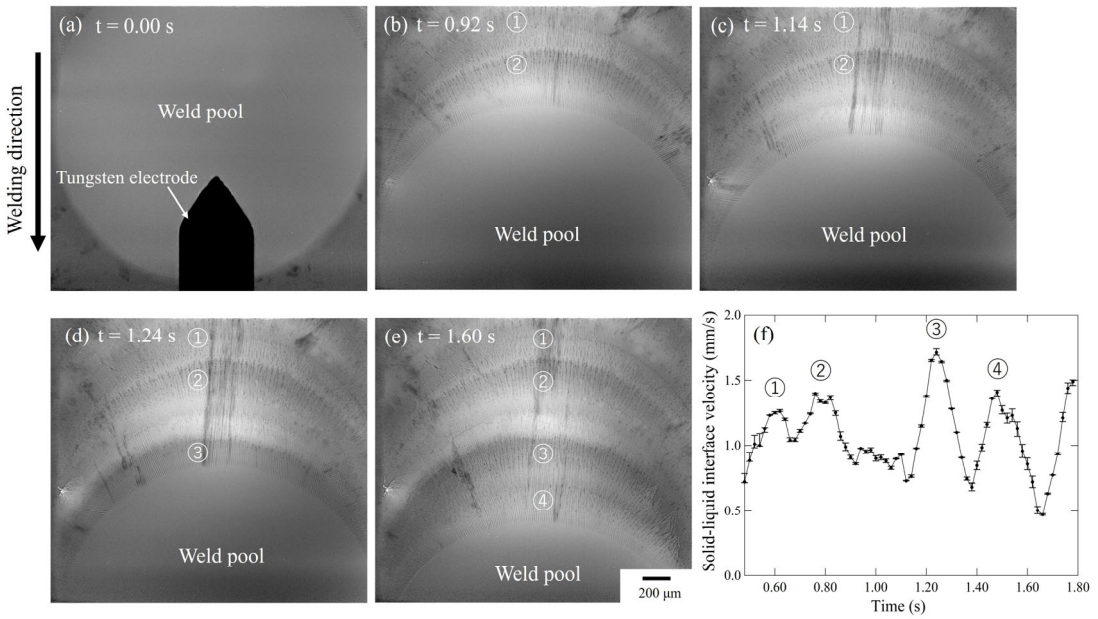

Figure 7. (a–e) Sequence of ripple formation at the welding speed of 1 mm/s. (f)Time dependence of solid-liquid interface velocity at the center position where each number corresponds to that in (b–e).

growth velocity decreased significantly, a solute-enriched band with a darker contrast image did not appear.

EPMA analysis was conducted to confirm the solute distribution of the solute-enriched bands. Figure 8(a) shows the microstructure of the quenched specimen. The EPMA mappings of Mn, Ni, and Si are shown in Figure 8(b–d). It can be seen that the Mn, Ni, and Si were segregated in the interdendritic regions. A semicircular band with a low solute concentration, which corresponds to the region between the two dotted white lines, was observed (Figure 8(b–d)). The solute distribution for the black dotted square in Figure 8(b) was further examined using EPMA at high spatial resolution. Figure 8(e) shows the microstructure consisting of columnar grains with high and low solute concentrations. The EPMA mappings of Mn, Ni, and Si are shown in Figure 8(f–h), respectively. It was found that Mn, Ni, and Si were segregated in the dendrite trunks and interdendritic regions within the solute-enriched band, as indicated by the white arrows in Figure 8(f). In the magnified image of Figure 8(i), the solute enrichment was observed clearly in the dendrite trunk. The average concentrations of Mn, Ni, and Si in the dendrite trunk were approximately 23, 28, and 38% higher, respectively, than those in the dendrite

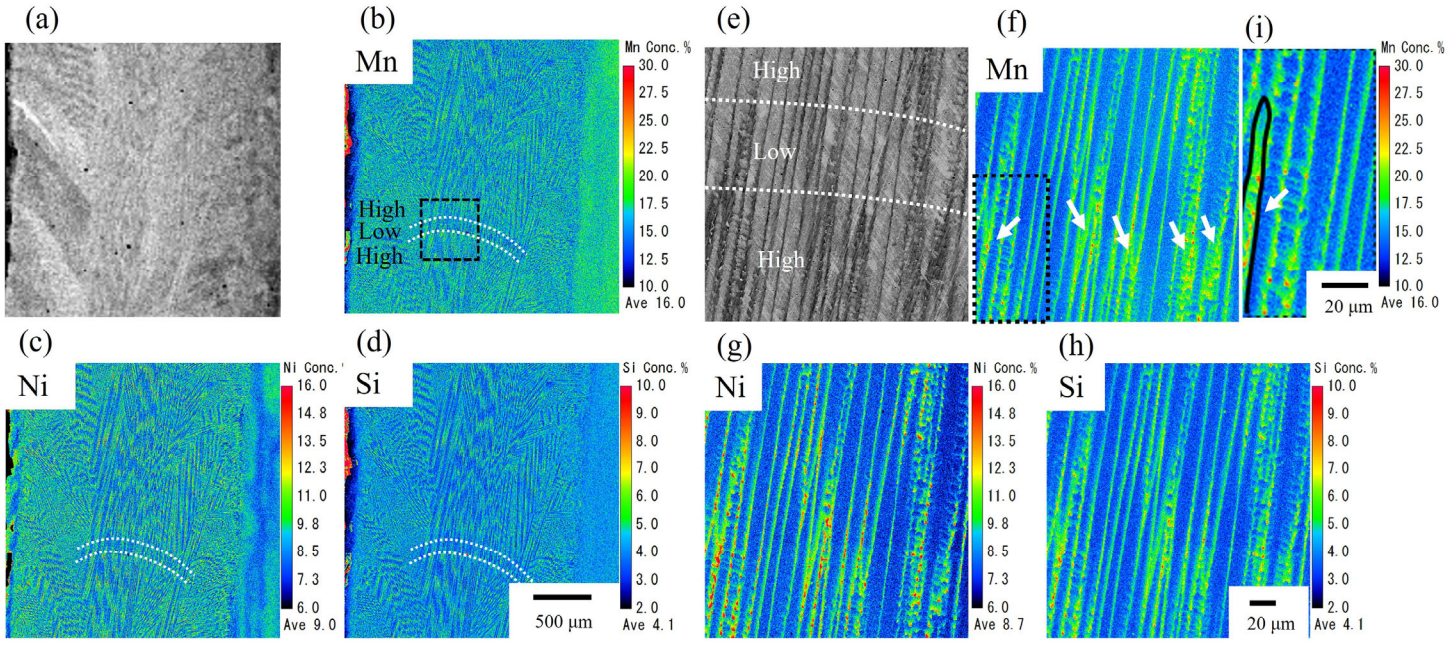

Figure 8. (a) Microstructure of the quenched specimen and EPMA mappings of (b) Mn, (c) Ni, and (d) Si. (e) Microstructure of the mapped area in black dotted square of (b) and EPMA mappings of (f) Mn, (g) Ni, and (h) Si at high spatial resolution. (i) Magnified image of the black dotted square in (f) where grain boundary is traced black.

trunk within the band with low solute concentrations. In contrast to welding, the cast Fe-Mn-Cr-Ni-Si alloy showed that Mn, Ni, and Si were segregated only in the interdendritic regions [24].

Attorre et al. [4] discussed the formation mechanism of solute bands. Assuming that the solidification progresses at a planar solid-liquid interface, the solute boundary layer δ is estimated by [25]

$$\delta = 2D/V \qquad (5)$$

where D is the diffusion coefficient of the solutes and V is the growth velocity. The rapid increase in the solid-liquid interface velocity causes a decrease in the amount of solute that can be enriched in the liquid owing to the decrease in the solute boundary layer. This results in solute damping into the dendrite trunk, where the solutes are enriched. Meanwhile, the amount of solute in the solidifying solid decreases with a decrease in the solid-liquid interface velocity. Consequently, a solute-enriched band is formed by fluctuations in the solid-liquid interface velocity. In this study, solute-enrichment in the dendrite trunk was likely attributed to solute dumping into the solidifying solid, induced by the rapid increase in the solid-liquid interface.

4. Conclusions

Time-resolved and in situ observations of curved columnar grain growth and ripple formation for an Fe-Mn-Cr-Ni-Si alloy during GTA melt-run welding were conducted using synchrotron radiation X-rays. The formation mechanism of the curved columnar grains was elucidated based on primary and secondary dendrite arm growth. Detailed image analysis was conducted to examine the relationship between the solid-liquid interface velocity and the solute-enriched band.

The formation of curved columnar grains occurred because of the change in the growth direction of the columnar dendrites via the development of secondary dendrite arms into new primary dendrite arms during GTA melt-run welding. The growth of primary dendrite arms became difficult owing to the blocking of other dendrites when θ exceeded 44º–49º at welding speeds of 1–7 mm/s. Consequently, secondary dendrite arms developed at higher growth velocities. In situ observations using X-ray imaging and detailed image analysis demonstrated that the growth velocity of the solid-liquid interface changed periodically, and a rapid increase in the interface velocity caused the formation of a solute-enriched band. EPMA analysis showed that the solute enrichment occurred in the dendrite trunk within the solute-enriched band.

Acknowledgements

The experiments were performed with the approval of the Japan Synchrotron Radiation Research Institute (JASRI) (Proposal Nos., 2023A1131, 2023B1201, 2024A1129, and 2024B1295).

Disclosure statement

No potential conflict of interest was reported by the authors.

References

[1] Kou S, Le Y. Welding parameters and the grain structure of weld metal – A thermodynamic consideration. Metall Trans A 1988;19a:1075–1082. doi:10.1007/BF02628392

[2] David SA, Vitek JM. Correlation between solidification parameters and weld microstructure. Int Mater Rev. 1989;34:213–245. doi:10.1179/imr.1989.34.1.2

[3] Kotecki DJ, Cheever DL, Howden DG. Mechanism of ripple formation during weld solidification. Weld J. 1972;51:368.

[4] Attorre DR, Parker JD, Williams NT. Mechanism of formation of solute bands in resistance seam welds of mild steel. Mater Sci Technol. 1996;12:697–703. doi:10.1179/mst.1996.12.8.697

[5] Hall AC, Robino CV. Association of microstructure features and rippling phenomenon in 304 stainless steel gas tungsten arc welds. Sci Tech Weld Join. 2004;9:103–108. doi:10.1179/136217104225017008

[6] Miyagi M, Wang H, Yoshida R, et al. Effect of alloy element on weld pool dynamics in laser welding of aluminum alloys. Sci Rep. 2018;8:12944. doi:10.1038/s41598-018-31350-4

[7] Aucott L, Huang D, Dong HB, et al. Initiation and growth kinetics of solidification cracking during welding of steel. Sci Rep. 2017;7:40255. doi:10.1038/srep40255

[8] Aveson JW, Reinhart G, Billia B, et al. Observation of the initiation and propagation of solidification cracks by means of in situ synchrotron X-ray radiography. IOP Conf S Mater Sci Eng. 2012;33:012040. doi:10.1088/1757-899X/33/1/012040

[9] Nagira T, Yamashita D, Kamai M, et al. In situ observation of solidification crack propagation for type 310S and 316L stainless steels during TIG welding using synchrotron X-ray imaging. J Mater Sci. 2021;56:10653–10663. doi:10.1007/s10853-021-05969-0

[10] Babu SS, Elmer JW, Vitek JM, et al. Time-resolved X-ray diffraction investigation of primary weld solidification in Fe-C-Al-Mn steel welds. Acta Mater. 2002;50:4763–4781. doi:10.1016/S1359-6454(02)00317-8

[11] Terasaki H, Komizo Y, Yonemuira M, et al. Time-resolved in-situ analysis of phase evolution for the directional solidification of carbon steel weld metal. Metall Mater Trans A. 2006;37:1261–1266. doi:10.1007/s11661-006-1077-8

[12] Nagira T, Nakamura T, Yoshinaka F, et al. Direct observation of solidification behaviors of Fe-Mn-Si alloys during arc spot welding using synchrotron X-ray. Scr Mater. 2022;216:114743. doi:10.1016/j.scriptamat.2022.114743

[13] Sawaguchi T, Nikulin I, Ogawa K, et al. Designing Fe-Mn-Si alloys with improved low-cycle fatigue lives. Scr Mater. 2015;99:49–52. doi:10.1016/j.scriptamat.2014.11.024

[14] Han R, Dong W, Lu S, et al. Modeling of morphological evolution of columnar dendritic grains in the molten pool of gas tungsten arc welding. Comput Mater Sci. 2014;95:351–361. doi:10.1016/j.commatsci.2014.07.052

[15] Fukumoto S, Yoshioka Y, Iwasaki Y. Simulation of nucleation and growth of austenite in duplex stainless steels. Weld J. 2022;36:65–75. doi:10.1080/09507116.2022.2030532

[16] Kitano H, Nagira T, Yoshinaka F, et al. Development of a method to evaluate strain in weld solidification using in-situ observations with high-brightness synchrotron X-rays. STAM: Methods. 2024;4:2403964. doi:10.1080/27660400.2024.2403964

[17] Haralick RM, Shanmugam K, Dinstein I. Textural Features for Image Classification. IEEE Trans Syst. 1973;SMC-3:610-621. doi: 10.1109/TSMC.1973.4309314

[18] Katayama S. Solidification phenomena of weld metals (1st report). Characteristic solidification morphologies, microstructures and solidification theory. Weld Int. 2000;14:939–951. doi:10.1080/09507110009549297

[19] Senda T, Matsuda F, Kato M, et al. Mechanism of weld solidification and behavior of its structure. J Jpn Weld Soc. 1971;40:242–250. doi:10.2207/qjjws1943.40.242

[20] Rappaz M, Gandin ChA. Probabilistic modelling of microstructure formation in solidification processes. Acta Metall Mater. 1993;41:345–360. doi:10.1016/0956-7151(93)90065-Z

[21] Trivedi R, David SA, Eshelman MA, et al. In situ observations of weld pool solidification using transparent metal-analog systems. J Appl Phys. 2003;93:4885–4895. doi:10.1063/1.1559934

[22] Kurz W, Bezençon C, G¨aumann M. Columnar to equiaxed transition in solidification processing. Sci Technol Adv Mater. 2001;2:185–191. doi:10.1016/S1468-6996(01)00047-X

[23] Xiao YH, Ouden G. A study of GTA weld pool oscillation. Weld J. 1990;69:289–293.

[24] Takamori S, Yoshinaka F, Hibaru T, et al. Effect of heat treatment on casting

microstructure and material properties of Fe-15Mn-10Cr-8Ni-4Si seismic damper alloy. J JFS. 2023;95:23–29. doi:10.11279/jfes.95.23

[25] Kurz W, Fisher DJ. Fundamentals of solidification, Fourth revised edition. Trans Tech Publications, Switzerland, 1998, p.187–189.